Hollow STW-Type Zeolite Single Crystals with Aluminum Gradient for Highly-Selective Production of p-Xylene from Methanol-Toluene Alkylation

Feng Jiao, Pengyao Yu, Yuchen Cui, Hao Li, Qing Hu, Yanan Xu, Svetlana Mintova, Hailing Guo, Hongbin Du

Hollow STW-Type Zeolite Single Crystals with Aluminum Gradient for Highly-Selective Production of *p*-Xylene from Methanol–Toluene Alkylation

Feng Jiao,[a] Pengyao Yu,[b] Yuchen Cui,[b] Hao Li,[a] Qing Hu,[a] Yanan Xu,[a] Svetlana Mintova,[c] Hailing Guo,*[b] and Hongbin Du*[a]

[a] F. Jiao, H. Li, Q. Hu, Y. Xu, and Prof. H. Du
State Key Laboratory of Coordination Chemistry, and School of Chemistry and Chemical Engineering
Nanjing University
Nanjing, 210023 (China)
E-mail: guohl@upc.edu.cn, hbdu@nju.edu.cn

[b] P. Yu, Y. Cui, and Prof. H. Guo
State Key Laboratory of Heavy Oil Processing, College of Chemical Engineering
China University of Petroleum (East China)
Qingdao 266580, Shandong, China

[c] Prof. S. Mintova
Laboratoire Catalyse et Spectrochimie (LCS)
Normandie Université
ENSICAEN, UNICAEN, CNRS, 6 Boulevard Maréchal Juin, Caen 14050, France

Supporting information for this article is given via a link at the end of the document.

Abstract: Zeolites with uniform micropores are important shape-selective catalysts. However, the external acid sites of zeolites have the negative impact on shape-selective catalysis, and the sole microporosity may lead to serious diffusion limitation. Herein, we report on direct synthesis of hierarchical hollow STW-type zeolite single crystals with siliceous exterior. In an alkalinous fluoride medium, the nucleation of highly siliceous STW zeolite takes place first, and the nanocrystals are preferentially aligned on the outer surface of the gel agglomerates to grow into single crystalline shells upon crystallization. The lagged crystallization of the internal Al-rich amorphous gels onto the inner surface of nanocrystalline zeolite shells lead to the formation of hollow cavities in the core of the zeolite crystals. The hollow zeolite single crystals possess low-to-high aluminum gradient from the surface to the core, resulting in an intrinsic inert external surface, and exhibit superior catalytic performance in toluene methylation reactions.

Introduction

Zeolites with regular molecular-size pores, high specific surface area, and good thermal / hydrothermal stability have been widely used as catalysts in the chemical industry.[1] The uniform micropores within the zeolites endow them with high shape-selective catalytic properties in various chemical processes. Of particular interest to the industry is the selective production of *p*-xylene from catalytic toluene alkylation with methanol (TAM), which is a vital feedstock for the production of terephthalic acid and terephthalate-based polymers. It is extremely challenging to achieve high *p*-xylene selectivity due to the thermodynamic equilibrium of the TAM reactions producing three xylene isomers of similar sizes. HZSM-5 is a well-known shape-selective zeolite that shows very high selectivity toward *p*-xylene when its channels are modified by P, B, Mg, and La to reduce pore size, though at the expense of activity loss due to the partially blocked pore openings.[2] Moreover, *p*-xylene selectivity can also be improved by increasing diffusion resistance of xylene isomers in the channel, for instance, by increasing crystal size or varying crystal shape to expose sinusoidal channel of ZSM-5 zeolite.[3] However, the increase in diffusion resistance limits the diffusion rate of reactants and products, which often results in coke formation and catalyst deactivation.[3a, 4] In addition, it is demonstrated that ZSM-5/silicalite-1 core-shell structured zeolite or inversely Al-zoned ZSM-5 zeolite with a siliceous exterior is beneficial for selectivity and diffusion,[5] due to the decrease in acid sites on the external surface, where non-shape-selective catalytic reactions occur.[3c, 6] However, these zeolites usually are not small single crystals but intergrown polycrystals, and the intracrystalline diffusion barriers from structural mismatch and large crystals often lead to diffusion restrictions.[7]

The hierarchical zeolites containing micropores and mesopores and even macropores can effectively overcome mass transport limitations.[8] Those materials are usually prepared by direct synthesis with high-cost mesoporogens as templates, consisting of polycrystalline aggregates of small crystallites.[9] The prominent external surface acid sites of hierarchical zeolite catalysts greatly reduce product selectivity.[10] Therefore, it is highly desirable to design and develop single-crystalline hierarchical zeolites with inert siliceous exteriors which would have fast mass transfer together with high selectivity.

Herein we report the direct synthesis of single-crystalline hierarchical aluminosilicate STW zeolite which possesses a chiral helix channel system with medium-size pores similar to the sinusoidal channels of ZSM-5.[11] The hierarchical STW zeolite consists of hollow single crystals with high crystallinity, uniform nanometer particle size, and good thermal stability. More importantly, the hollow STW nanocrystals show low-to-high composition gradient of aluminum distribution from the surface to the core. High *p*-xylene selectivity and stability in the catalytic toluene alkylation with methanol over the hierarchical STW zeolites are measured.

Results and Discussion

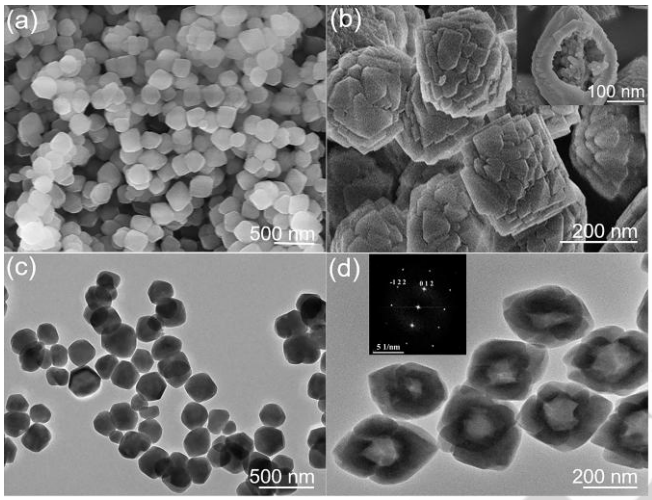

Figure 1. SEM images of samples Al-STW-s (a) and Al-STW-h (b). Inset in (b) shows the broken hollow structure of a crystal. TEM images of samples Al-STW-s (c) and Al-STW-h (d). Inset in (d) shows the corresponding Fast Fourier-Transformed diffractogram from a whole zeolite crystal.

Aluminosilicate STW zeolite was obtained from a gel with molar ratios of 1 SiO_2 : 1 SDA(OH) : *x* HF : 0.003 Al_2O_3 : 5 H_2O at 160°C for 15 days. As structure-directing agent (SDA), a 1-methyl-1,5-diazabicyclo[4.3.0]non-5-ene (MDBN) cation was used.[12] Detailed synthesis conditions are reported in Table S1. The samples with STW-type framework structure were synthesized as confirmed by powder X-ray diffraction (PXRD) (Figure S1). Scanning electron microscopy (SEM) and transmission electron microscopy (TEM) images show that the samples exhibit diverse morphology depending on the synthesis conditions. The sample named Al-STW-n prepared under normal conditions with an equivalent amount of SDAOH and HF (Run 1, *x* = 1, Table S1) consists of regular hexagonal-bipyramid crystals with a size of ca. 3 μm in length (Figure S2), while uniform nanocrystal zeolite named as Al-STW-s (Figure 1a and 1c) was synthesized by use of zeolite STW seeds to promote fast nucleation and crystal growth (Run 2, Table S1), similar to fluoride-free synthesis of siliceous STW.[12] Hierarchical hollow STW zeolite, sample named as Al-STW-h was synthesized (Run 3, *x* = 0.3, Table S1) by simply reducing the amount of HF used in the synthesis. SEM images show that the Al-STW-h consists of uniform intergrown hexagonal-bipyramid crystals of ca. 300 nm in diameter with hollow structure (Figure 1b). TEM images clearly reveal that all crystals are hollow, possessing a large inner cavity (ca. 100-150 nm in length) and the shell thickness is of approximately 40-70 nm (Figure 1d). The single-crystalline nature of Al-STW-h is confirmed by the electron diffraction pattern (Figure 1d) and high-resolution TEM image (Figure S3); a distinct single set of diffraction spots and continuous zeolite microporous structure are clearly seen.

The highly-crystalline single crystals of the Al-STW-h show high thermal and hydrothermal stability (Figure S4). In contrast, the hierarchical zeolites obtained by post-synthesis approach usually exhibit poor stability.[13] Solid state ^{29}Si and ^{27}Al NMR spectra of samples Al-STW-s and Al-STW-h show that the Si and Al atoms are tetrahedrally coordinated (i.e. $Si(OSi)_4$ and $Si(OSi)_3(OAl)$, $Al(OSi)_4$, respectively) (Figures S5 and S6). Nitrogen adsorption–desorption isotherms of samples Al-STW-s and Al-STW-h are both of type-I (Figure S7), characteristic of microporous materials, and contain adsorption hysteresis type H4 and H3 indicating the presence of mesopores and macropores within the aggregated and intergrown STW nanocrystals, respectively. Pore size distribution analyses based on density-function-theory (DFT) model show the presence of noticeable mesopores and macropores in sample Al-STW-h, resulting in total pore volume of 0.333 $cm^3\ g^{-1}$ larger than that of Al-STW-s (0.223 $cm^3\ g^{-1}$), but slightly smaller Brunauer–Emmett–Teller (BET) surface area (509 $m^2\ g^{-1}$ vs 551 $m^2\ g^{-1}$) (Table S2).

The incorporation of aluminum in zeolite STW framework creates acidic sites and renders it as a good candidate for shape-selective catalysis. The acidic properties of samples Al-STW-s (Si/Al = 97) and Al-STW-h (Si/Al = 89) were studied by comparison with nanozeolite H-ZSM-5 with a Si/Al ratio of 93 and particle size of ca. 200 nm (reference sample named ZSM-5-n93, Figure S8). As shown in Figure S9, ammonia temperature-programmed desorption (NH_3-TPD) curves of the three samples display three peaks at 160°C, 250°C, and 380°C, corresponding to NH_3 desorption from weak, medium-strong, and strong acid sites,[14] respectively. The desorption temperature for the reference sample, ZSM-5-n93 at strong acid sites is higher (398°C vs 372°C for Al-STW) and the peak intensity is larger than those for the two Al-STW samples, demonstrating that ZSM-5-n93 possesses stronger and more acid sites. The acid properties of Al-STW-h is similar to those of Al-STW-s (Table S3).

The acid properties of samples Al-STW-s and Al-STW-h were further studied by diffuse reflectance infrared Fourier-transformed spectroscopy (DRIFTS) using pyridine (Py) and 2,6-di-tert-butylpyridine (DTBPy) probe molecules adsorbed at 150, 250 and 350°C. The bands at 1452 and 1544 cm^{-1} in the Py-DRIFTS spectra are assigned to pyridine adsorbed on Lewis (L) acid sites and Brönsted (B) acid sites, respectively (Figure 2).[14b] Despite having the smallest BET surface area of 413 $m^2\ g^{-1}$, the ZSM-5-n93 zeolite displays the largest peak areas as measured at the three temperatures (Table S4), suggesting the presence of the most acidic sites amongst the three samples. The B/L ratio of ZSM-5-n93 increases from 3.25 to 5.53 along with

increasing of temperature, proving that the ZSM-5-n93 is a strong Brönsted acid catalyst. The number of accessible B acid sites in Al-STW-s is approximately 53% of those in ZSM-5-n93 at 150°C and 51% at 250 and 350°C. Interestingly, the Al-STW-h possesses more accessible B-acid sites than the Al-STW-s, ca. 64% at 150°C and 62% of those in ZSM-5-n93 at 250 and 350°C; this can be explained by its hollow hierarchical structure. Both Al-STW-h and Al-STW-s zeolites show same decline trend for the B/L ratio with the increase of temperature (Figure S10), in contrast to the ZSM-5-n93. Noticeably, the numbers of the accessible L-acid sites in samples Al-STW-h and Al-STW-s measured at 250 and 350°C are comparable to those of ZSM-5-n93.

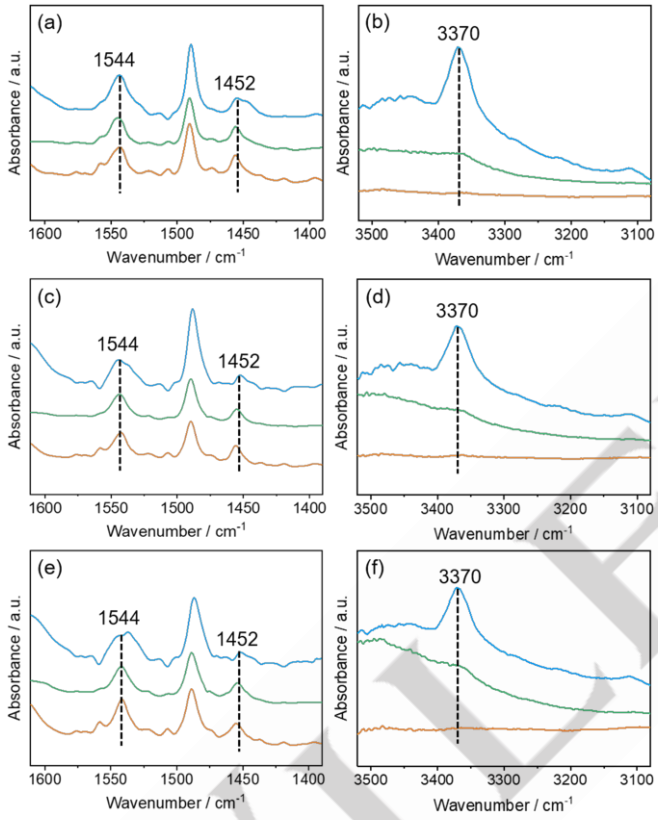

Figure 2. Py-DRIFTS (a, c, and e) and DTBPy-DRIFTS (b, d, and f) spectra of ZSM-5-n93 (blue line), Al-STW-s (green line) and Al-STW-h (orange line) at the desorption temperature of 150°C (a and b), 250°C (c and d), 350°C (e and f).

The external acid sites of the three samples were characterized by adsorption of 2,6-di-*tert*-butylpyridine (DTBPy), a large molecule that cannot enter the 10-member-ring (10-MR) channels of zeolites. A band at ca. 3370 cm^{-1} characteristic for the adsorbed $DTBPyH^+$ ions, is used to monitor the B acid sites.[15] As shown in Figure 2, the intensities of the band at 3367 cm^{-1} for ZSM-5-n93 are greater than those for Al-STW-s and Al-STW-h at all three temperatures, thus proving that the ZSM-5-n93 has more abundant external surface acid sites attributing to the larger external surface area (26.4%, see Table S2). The presence of very weak peak at 3367 cm^{-1} in sample Al-STW-s indicates few external acid sites owing to its low external surface area (7.3%, see Table S2), while the spectrum of Al-STW-h sample contains no peak at 3367 cm^{-1}, suggesting almost zero external surface acidity. The weak or absence of external acidity in Al-STW-s and Al-STW-h samples was confirmed by catalytic test in benzylation of toluene (Figure S11). The reaction was selected since it occurs on the external surface due to inaccessibility of the 10-memebred ring pores in the catalysts. The measured conversion of 64.5%, 15.6% and 11.4% for samples ZSM-5-n93, Al-STW-s and Al-STW-h, respectively, is in accordance with their external surface acidity.

The absence of external acidity in sample Al-STW-h is attributed to extremely low aluminum content on the external surface of zeolite particles, which was confirmed by Ar-ion sputtering X-ray photoelectron spectroscopy (XPS) analyses. As shown in Figure 3a, the Al 2p XPS signal on the external surface of sample Al-STW-h is extremely low, and it increases from the surface to the core of the crystals upon increasing the Ar-ion etching time. The Si/Al ratio of sample Al-STW-h gradually decreases from the surface to the core of the crystals (Figure 3b), demonstrating that aluminum in Al-STW-h is unevenly distributed, with the composition gradient of extremely low Al concentration on the surface of zeolite crystals and high in the core. The inversely zoned Al distribution of Al-STW-h was further confirmed by scanning transmission electron microscopy (STEM) and energy dispersive spectroscopy (EDS) (Figure 3c). In comparison, sample Al-STW-s has nearly homogeneous aluminum distribution within the zeolite crystals (Figure S12). Zeolites with chemical composition gradient mostly observed in large single zeolite crystals have been reported.[3c, 16] The formation of hollow Al-STW-h nanocrystals with Al gradient is rather rare.

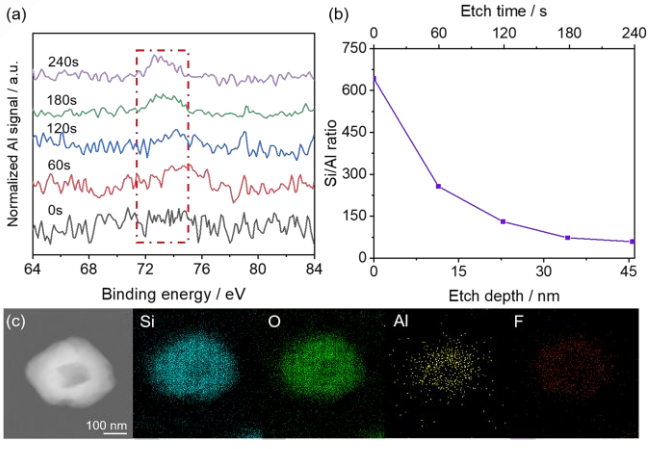

Figure 3. Evolution profiles of (a) normalized Al 2p XPS peak intensity with Ar-ion sputtering time, and (b) the Si/Al ratio as a function of Ar-ion etch depth and etch time of Al-STW-h. (c) STEM-EDS mapping images of Al-STW-h: Si (blue), O (green), Al (yellow), and F (red).

The morphology evolution of sample Al-STW-h synthesized at different crystallization time is shown in Figure 4. At the initial

crystallization stage (1 day), the precursor formed uniform wormlike nanoparticles of about 30 × 70 nm^2 in size (Figure 4a, 4f). The PXRD analyses showed that precursor nanoparticles were amorphous (Figure S13). After further incubation, the nanoparticles aggregated and formed larger agglomerates, where

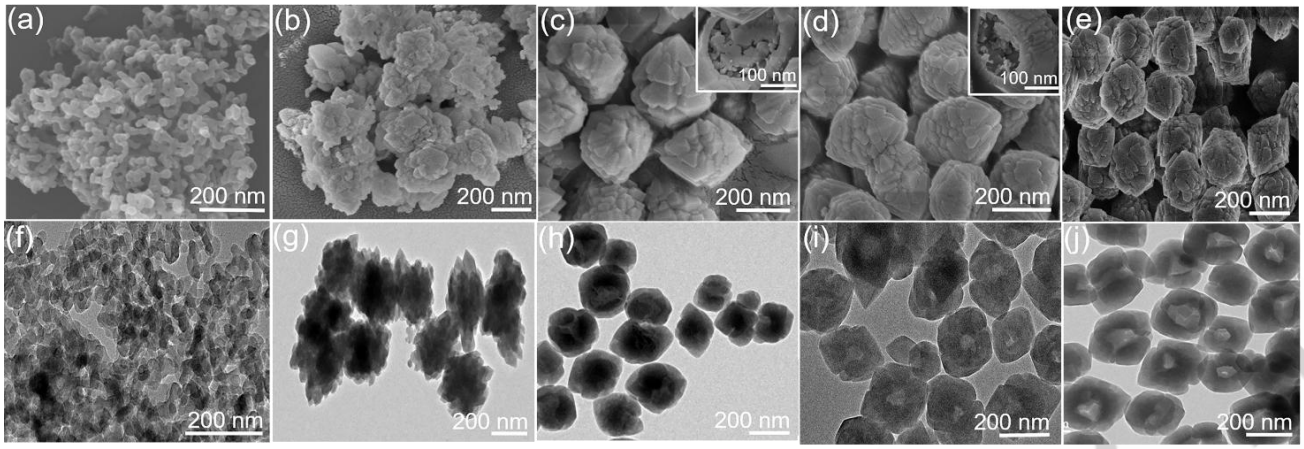

Figure 4. SEM and TEM images of sample Al-STW-h synthesized for different time: 1 d (a, f), 4 d (b, g), 8 d (c, h), 12 d (d, i), and 15 d (e, j). *Insets* in (c) and (d) show broken crystals.

the crystal nucleation and growth began.[17] SEM and TEM images showed the appearance of aligned zeolite nanocrystals on the periphery of the agglomerates after 4 days, while the inner core was still amorphous as evidenced by PXRD and selected-area electron diffraction (SAED) patterns (Figures 4b, 4g, S13 and S14). This is in accordance with the observations that zeolite crystals nucleate on the periphery of the aggregated amorphous gels.[18] Interestingly, the agglomerates exhibited aluminum concentration gradient, with the surface STW zeolite nanocrystals being highly siliceous (Si/Al ≈ 583) and the amorphous core being Al-rich (Si/Al ≈ 76) (Figure S14). Upon further crystallization, the agglomerates' shape became regular (bipyramid-like type) and the surface turned smoother, but the interior was disordered as demonstrated (see sample obtained after 8 days, Figure 4c, 4h). As crystallization time increased from 8 to 12 days, hollow cavities inside the agglomerates appeared while the overall size of the agglomerates remained approximately constant (Figures 4d, 4i and S13); this suggests that the nutrients for the crystal growth were primarily supplied by the inside of the agglomerates. With the crystallization time increasing from 12 to 15 days, the internal gel nutrients within the agglomerates were continuously crystallized, leaving larger inner cavities (Figure 4e, 4j). In comparison, the crystallization of Al-STW-s is different from that of Al-STW-h. With the help of seeds, the crystal nucleus of Al-STW-s formed rapidly and grew into regular single crystals (Figure S15 and S16).

The different crystallization profiles of Al-STW-s and Al-STW-h suggested that the formation of Al-STW-h zeolite was likely due to its unique synthetic gel compositions with an alkalinous fluoride medium (F^-/OH^- = 0.3). It is known that the fluoride ion is favorable to the crystallization of zeolite STW zeolite.[12] Additional experiments showed that the siliceous STW zeolite began to crystallize after 1 d under similar conditions, much faster than the Al-rich STW (Figure S17). Therefore, we postulated that during the crystallization of Al-STW-h, the nucleation and crystal growth of highly siliceous F-rich STW zeolite took place first and preferentially on the outer surface of the gel agglomerates (Figure 3c and Scheme S1), where the soluble siliceous species and fluoride ions were more readily accessible. After depletion of the soluble nutrients, the highly siliceous STW zeolite nanocrystals on the surface of the agglomerates started to act as seeds to facilitate the crystallization of the F-deficient, Al-rich gels in the core. The crystallization of the internal loosely-packed Al-rich amorphous gels onto the inner surface of zeolite nanocrystal shells led to the formation of the Al-gradient zeolite crystals, and also created hollow cavities in the core of the zeolite crystals. Single crystals of Al-STW-h were formed as a result of oriented attachment and intergrowth of adjacent nanocrystals within each agglomerate.[19]

The crystallization process of Al-STW-h can also be inferred from the porosity of the samples at different stages (Figures S18 and S19, Table S5). Pore size distribution profiles showed the appearance and increase in proportion of the uniform micropores of 5.6 Å in diameter, indicative of the nucleation and growth of zeolite STW. Upon increasing the crystallization time, the disordered mesopores of 2-200 nm owing to the presence of amorphous species gradually disappeared. Prolonged crystallization led to the reappearance of mesopores and macropores, due to the formation of inner cavities within zeolite crystals (Figure S19).

The catalytic performance of Al-STW on TAM reaction was evaluated by comparison with that of MFI catalysts. As shown in Figure 5, Al-STW-s showed a high *p*-xylene selectivity of 90%, which is mainly attributed to its weak external acidity because of low external/total (E/T) surface ratio of 7.3% (Table S2). Another reason is the unique topological feature of the STW zeolite consisting of helical 10-MR channels (5.8 × 5.5 $Å^2$) and straight 8-MR channels (4.5 × 3.2 $Å^2$). The latter is too small for most aromatics to pass through. The helical 10-ring channels are primarily responsible for high *p*-xylene selectivity, as the zigzag (sinusoidal) channels have been proven to improve the shape-selectivity for *p*-xylene.[3c, 3d, 20] However, Al-STW-s exhibited a

low toluene conversion of ca. 11.3% and gradually deactivated after 10 h of reaction. That is due to the one-dimensional 10-MR pore system of the STW zeolite more easily blocked by coking. In comparison, ZSM-5-n93 exhibited a higher toluene conversion (23.5%) and longer catalytic life (24 h), which is attributed to its remarkable acidity and the two-dimensional 10-MR channels. However, ZSM-5-n93 showed a low *p*-xylene selectivity of ca. 30%, close to the thermodynamic equilibrium of xylene isomers (~24%),[3c, 21] owing to its prominent external acidity (Table S2). Nanozeolite H-ZSM-5 (Si/Al = 138, named as ZSM-5-n138) with less amount of strong acidity (131 μmol g^{-1}, similar to Al-STW-s and Al-STW-h with 118 and 127 μmol g^{-1}, respectively, see Figure S20 and Table S3) displayed a slightly higher *p*-xylene selectivity of 48.6% and improved catalytic lifetime (35 h) than ZSM-5-n93 (Figure S21). Moreover, core-shell structured ZSM-5@silicalite-1 (Si/Al = 90, named ZSM-5@S1, Figure S22 and S23) showed a higher *p*-xylene selectivity of 98.7% , a longer lifetime of 57 h, but a lower conversion of ca. 15%. The increase in *p*-xylene selectivity and lifetime from ZSM-n93 to ZSM-n138 to ZSM-5@S1 is mainly attributed to the decrease in external surface acidic sites (Figure S24), where the non-shape-selective reactions occur. The reduction of external acidic sites reduces generation of larger coke-forming aromatic species such as C_{9+} (Figure S25), thereby reducing deactivation.[5] Interestingly, Al-STW-h showed a high *para*-selectivity of ca. 93%, attributed to negligible external acidity caused by siliceous exterior. More importantly, Al-STW-h displayed a higher toluene conversion of 17.5% and a much longer lifetime of over 85 h than Al-STW-s or ZSM-5@S1. In contrast, the *para*-selectivity over the crushed Al-STW-h (Figure S26) decrease to 40.8%, accompanied by decreased lifetime of ca. 30 h. The results strongly suggest that the siliceous exterior and single-crystalline hierarchical hollow structure of Al-STW-h catalyst played an important role in enhancing *para*-selectivity and lifetime.

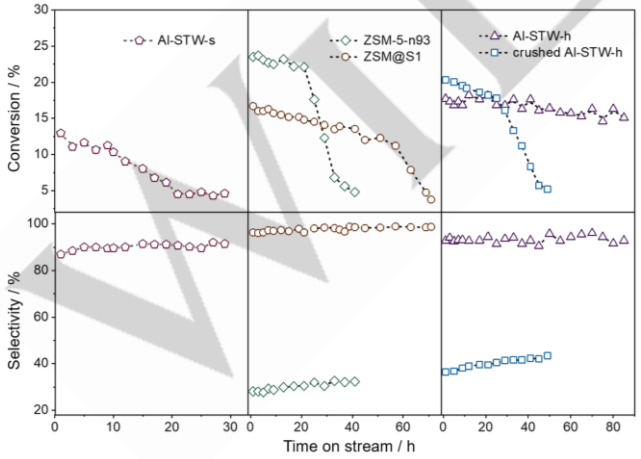

Figure 5. *p*-Xylene selectivity and toluene conversion over Al-STW-s, ZSM-5-n93, ZSM-5@S1, Al-STW-h, and crushed Al-STW-h catalysts at 400°C, 2.0 MPa, 2.5 h^{-1} WHSV, and a 3:1 toluene/methanol ratio.

To further elucidate the extraordinary performance of the Al-STW-h catalyst, characteristic diffusion timescale (R^2/D), a proxy for effective internal diffusion time, was derived from transient sorption experiments with 2,3-dimethylbutane (Figure S27 and S28).[22] The R^2/D value of Al-STW-h (2.3 ×10^3 s) is the smallest (Table S6), one order of magnitude smaller than that of ZSM-5@S1 (3.08 ×10^4 s). This indicates that diffusion in Al-STW-h is much faster than in ZSM-5@S1 despite they have similar crystallite sizes, Si/Al ratio and inert external surface acidity. It is likely that the intracrystalline diffusion barriers from structural mismatch and the sole microporosity in ZSM-5@S1 led to increased diffusion limitations and thus reduced lifetime in TAM reactions.[7] On the other hand, the single-crystalline, hierarchical hollow structure of Al-STW-h dramatically reduced the diffusion limitations, which led to an enhanced catalyst lifetime. In addition, the large inner cavities of Al-STW-h not only shortened the mass transfer path but also afforded more coke deposition. In a word, Al-STW-h zeolite displayed extraordinarily high *p*-xylene reactivity and long lifetime amongst the modified zeolites reported in literature (Table S7), making it a good candidate for TAM.

Conclusion

In summary, we demonstrate a new strategy for constructing hollow single crystals of STW-type aluminosilicate zeolite containing large cavity and nano-sized siliceous shell. The hollow zeolite crystals possess nearly zero acidity on the external surface due to low-to-high aluminum gradient distribution from the surface to the core. The intrinsic inert external surface and unique structural features of the STW-type aluminosilicate zeolite resulted in high *p*-xylene selectivity, activity and stability in toluene alkylation with methanol. This work not only opens up a new way to the synthesis of high-quality single-crystalline hollow zeolites, but also provides a synthesis strategy for regulating the Al gradient distribution in zeolites.

Supporting Information

Supporting information for this article is given via a link at the end of the document. The authors have cited additional references within the Supporting Information. [23-27]

Acknowledgements

This work was supported by the National Natural Science Foundation of China (22272076, 22071099, 22175200, and 21975285), the Fundamental Research Funds for the Central Universities (020514380293), and National Key Research and Development Program of China of Ministry of Science and Technology (2022YFE0116000).

Keywords: catalysts • composition gradient • hierarchical • single crystal • zeolites

[1] a) M. E. Davis, *Nature* **2002**, *417*, 813-821; b) Y. Tao, H. Kanoh, L. Abrams, K. Kaneko, *Chem. Rev.* **2006**, *106*, 896−910; c) A. Primo, H. Garcia, *Chem. Soc. Rev.* **2014**, *43*, 7548-7561.

[2] a) Y. Zhao, H. Wu, W. Tan, M. Zhang, M. Liu, C. Song, X. Wang, X. Guo, *Catal. Today* **2010**, *156*, 69-73; b) J. P. Breen, R. Burch, M. Kulkarni, D. McLaughlin, P. J. Collier, S. E. Golunski, *Appl. Catal. A-Gen.* **2007**, *316*, 53-60; c) Y. Zhao, W. Tan, H. Wu, A. Zhang, M. Liu, G. Li, X. Wang, C. Song, X. Guo, *Catal. Today* **2011**, *160*, 179-183; d) Z. Zhu, Q. Chen, W. Zhu, D. Kong, C. Li, *Catal. Today* **2004**, *93-95*, 321-325.

[3] a) Y. S. Bhat, J. Das, K. V. Rao, A. B. Halgeri, *J. Catal.* **1996**, *159*, 368-374; b) T. Kunieda, J.-H. Kim, M. Niwa, *J. Catal.* **1999**, *188*, 431-433; c) C. Wang, L. Zhang, X. Huang, Y. Zhu, G. K. Li, Q. Gu, J. Chen, L. Ma, X. Li, Q. He, J. Xu, Q. Sun, C. Song, M. Peng, J. Sun, D. Ma, *Nat. Commun.* **2019**, *10*, 4348-4355; d) D. Parmar, S. H. Cha, T. Salavati-Fard, A. Agarwal, H. Chiang, S. M. Washburn, J. C. Palmer, L. C. Grabow, J. D. Rimer, *J. Am. Chem. Soc.* **2022**, *144*, 7861-7870.

[4] S. Zheng, A. Jentys, J. A. Lercher, *J. Catal.* **2006**, *241*, 304-311.

[5] T. T. Le, W. Qin, A. Agarwal, N. Nikolopoulos, D. Fu, M. D. Patton, C. Weiland, S. R. Bare, J. C. Palmer, B. M. Weckhuysen, J. D. Rimer, *Nat. Catal.* **2023**, *6*, 254-265.

[6] a) D. Vanvu, M. Miyamoto, N. Nishiyama, Y. Egashira, K. Ueyama, *J. Catal.* **2006**, *243*, 389-394; b) M. Okamoto, Y. Osafune, *Micropor. Mesopor. Mat.* **2011**, *143*, 413-418.

[7] a) D. Mores, E. Stavitski, S. P. Verkleij, A. Lombard, A. Cabiac, L. Rouleau, J. Patarin, A. Simon-Masseron, B. M. Weckhuysen, *Phys. Chem. Chem. Phys.* **2011**, *13*, 15985-15994; b) L. Karwacki, M. H. Kox, D. A. de Winter, M. R. Drury, J. D. Meeldijk, E. Stavitski, W. Schmidt, M. Mertens, P. Cubillas, N. John, A. Chan, N. Kahn, S. R. Bare, M. Anderson, J. Kornatowski, B. M. Weckhuysen, *Nat. Mater.* **2009**, *8*, 959-965; c) G. D. Price, J. J. Pluth, J. V. Smith, J. M. Bennett, R. L. Patton, *J. Am. Chem. Soc.* **1982**, *104*, 5971-5977.

[8] a) S. Lopez-Orozco, A. Inayat, A. Schwab, T. Selvam, W. Schwieger, *Adv. Mater.* **2011**, *23*, 2602-2615; b) M. Hartmann, A. G. Machoke, W. Schwieger, *Chem. Soc. Rev.* **2016**, *45*, 3313-3330.

[9] a) X. Shen, W. Mao, Y. Ma, D. Xu, P. Wu, O. Terasaki, L. Han, S. Che, *Angew. Chem. Int. Ed.* **2018**, *57*, 724-728; *Angew.Chem.* **2018**, *130*, 732 –736; b) D. Xu, Y. Ma, Z. Jing, L. Han, B. Singh, J. Feng, X. Shen, F. Cao, P. Oleynikov, H. Sun, O. Terasaki, S. Che, *Nat. Commun.* **2014**, *5*, 4262.

[10] C. Fernandez, I. Stan, J. P. Gilson, K. Thomas, A. Vicente, A. Bonilla, J. Perez-Ramirez, *Chem. Eur. J.* **2010**, *16*, 6224-6233.

[11] L. Tang, L. Shi, C. Bonneau, J. Sun, H. Yue, A. Ojuva, B. L. Lee, M. Kritikos, R. G. Bell, Z. Bacsik, J. Mink, X. Zou, *Nat. Mater.* **2008**, *7*, 381-385.

[12] F. Jiao, J. Zhang, X. Cai, H. Li, Y. Xu, Y. Zhao, H. Du, *Chem. Commun.* **2023**, *59*, 1649-1652.

[13] a) K. Tarach, K. Góra-Marek, J. Tekla, K. Brylewska, J. Datka, K. Mlekodaj, W. Makowski, M. C. Igualada López, J. Martínez Triguero, F. Rey, *J. Catal.* **2014**, *312*, 46-57; b) K. A. Tarach, J. Martinez-Triguero, F. Rey, K. Góra-Marek, *J. Catal.* **2016**, *339*, 256-269.

[14] a) J. Zhang, X. Zhu, G. Wang, P. Wang, Z. Meng, C. Li, *Chem. Eng. J.* **2017**, *327*, 278-285; b) J. Zhang, W. Qian, C. Kong, F. Wei, *ACS. Catal.* **2015**, *5*, 2982-2988.

[15] A. Corma, V. Fornes, L. Forni, F. Márquez, J. Martınez-Triguero, D. Moscotti, *J. Catal.* **1998**, *179*, 451-458.

[16] R. v. Ballmoos, W. M. Meier, *Nature* **1981**, *289*, 782-783.

[17] a) T. M. Davis, T. O. Drews, H. Ramanan, C. He, J. Dong, H. Schnablegger, M. A. Katsoulakis, E. Kokkoli, A. V. McCormick, R. L. Penn, M. Tsapatsis, *Nat. Mater.* **2006**, *5*, 400-408; b) S. Mintova, N. H. Olson, V. Valtchev, T. Bein, *Science* **1999**, *283*, 958-960.

[18] a) S. Mintova, N. H. Olson, T. Bein, *Angew. Chem. Int. Ed.* **1999**, *38*, 3201-3204; b) V. P. Valtchev, K. N. Bozhilov, *J. Am. Chem. Soc.* **2005**, *127*, 16171-16177.

[19] J. J. De Yoreo, P. U. Gilbert, N. A. Sommerdijk, R. L. Penn, S. Whitelam, D. Joester, H. Zhang, J. D. Rimer, A. Navrotsky, J. F. Banfield, A. F. Wallace, F. M. Michel, F. C. Meldrum, H. Colfen, P. M. Dove, *Science* **2015**, *349*, aaa6760.

[20] Q. Chen, J. Liu, B. Yang, *Nat. Commun.* **2021**, *12*, 3725.

[21] M. Miyamoto, T. Kamei, N. Nishiyama, Y. Egashira, K. Ueyama, *Adv. Mater.* **2005**, *17*, 1985-1988.

[22] a) R. Khare, D. Millar, A. Bhan, *J. Catal.* **2015**, *321*, 23-31; b) Y. Shen, T. T. Le, D. Fu, J. E. Schmidt, M. Filez, B. M. Weckhuysen, J. D. Rimer, *ACS. Catal.* **2018**, *8*, 11042-11053.

[23] J. Crank, *The Mathematics of Diffusion*, Clarendon Press, **1975**, p. 414.

[24] M. Yu, J. Wyss, R. Noble, J. Falconer, *Micropor. Mesopor. Mater.* **2008**, *111*, 24-31.

[25] J. Karger, D. Ruthven, D. Theodorou, *Diffusion in Nanoporous Materials*, Wiley-VCH, Weintheim, **2012**, p. 872.

[26] J. Breen, R. Burch, M. Kulkarni, P . Collier, S. Golunski, *J. Am. Chem. Soc.* **2004**, *127*, 5020–5021.

[27] P . Lu, Z. Fei, L. Li, X. Feng, W. Ji, W. Ding, Y . Chen, W. Yang, Z. Xie, *Appl. Catal. A-Gen.* **2013**, *453*, 302-309.

Entry for the Table of Contents

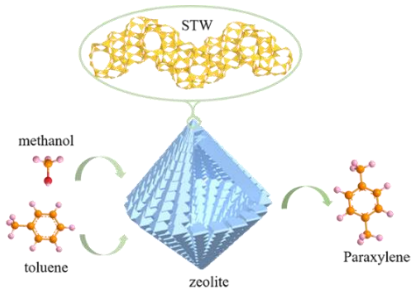

The hierarchical hollow single crystal STW-type zeolite was directly prepared in an alkalinous fluoride medium, which exhibits excellent catalytic performance in toluene methylation reactions to *p*-xylene.